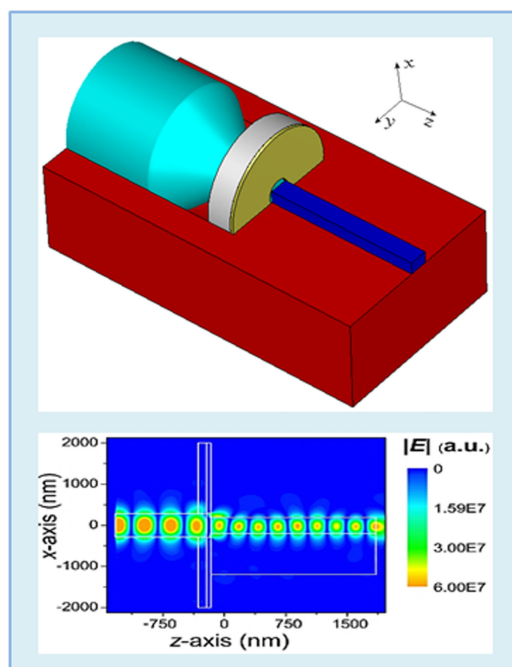


Efficient Background-Noise-Reduced Single-Mode Waveguides Platform for On-Chip Integrated Photonics

Volume 11, Number 1, February 2019

Yevhenii Morozov
Anatoly Lapchuk
Zichun Le
Ye-Fei Dong



DOI: 10.1109/JPHOT.2018.2885334
1943-0655 © 2018 IEEE

Efficient Background-Noise-Reduced Single-Mode Waveguides Platform for On-Chip Integrated Photonics

Yevhenii Morozov ^{1,2} Anatoly Lapchuk,² Zichun Le ¹,
and Ye-Fei Dong ¹

¹College of Science, Zhejiang University of Technology, Hangzhou 310023, China

²Institute for Information Recording, National Academy of Sciences of Ukraine, Kiev 03113, Ukraine

DOI:10.1109/JPHOT.2018.2885334

1943-0655 © 2018 IEEE. Translations and content mining are permitted for academic research only.

Personal use is also permitted, but republication/redistribution requires IEEE permission.

See http://www.ieee.org/publications_standards/publications/rights/index.html for more information.

Manuscript received October 26, 2018; revised November 30, 2018; accepted December 3, 2018. Date of publication December 6, 2018; date of current version December 28, 2018. This work was supported in part by the special funding of "The Belt and Road" International Cooperation of Zhejiang Province under Grant 2015C04005, in part by the National Natural Science Foundation of China under Grant 61571399, and in part by the R&D Funding of NAS of Ukraine under Grant 0114U002061. Corresponding author: Zichun Le (e-mail: lzc@zjut.edu.cn). This paper has supplementary downloadable material available at <http://ieeexplore.ieee.org>, provided by the authors.

Abstract: In this paper, we propose a modified platform for on-chip integrated photonics. The platform allows one to efficiently connect a tapered optical fiber or fiber lens to an on-chip waveguide with high alignment precision and to mechanically fix the fiber on the chip to prevent defocusing, lateral shift, and angular detuning during device operation. The metal screen of the connector—made of gold—prevents any penetration of the background radiation into the optical circuit, something which is not possible to achieve in all the cases using tapers or grating couplers. We performed impedance-matching analysis based on transmission line theory and numerically optimized the platform, allowing us to achieve a tapered fiber mode to on-chip waveguide mode transformation efficiency as high as 96% (−0.177 dB) at wavelengths of 785 and 1550 nm. The platform bandwidth (transformation efficiency $\geq 80\%$) is 151 nm. At the same time, transformation efficiency is stable (reduction less than 1%) in an offset range of ± 2 nm—enough for modern on-chip and off-chip coherent light sources. The horizontal and vertical lateral alignment tolerances for the platform are 700 and 600 nm, respectively, at a transformation efficiency $\geq 80\%$ while the longitudinal alignment tolerance is approximately 70 nm. Due to the relatively high lateral and longitudinal tolerances, it is possible to produce the platform at high efficiency using existing fabrication nanotechnologies. We believe that this platform accelerates the realization of fully on-chip Raman spectrometers and may be of practical importance in other on-chip integrated photonic devices.

Index Terms: Connectors, design optimization, energy efficiency, noise cancellation, numerical simulation, photonic integrated circuits, silicon-on-insulator, system-on-chip.

1. Introduction

Photonic integrated circuits made of light sources [1], modulators and switches [2], [3], filters [4], and different types of routing devices such as silicon (Si) and silicon nitride (Si_3N_4) waveguides [5]–[8] play a crucial role in the creation of fully on-chip optical communication devices [9], high-performance computing [10], and emerging fields of lab-on-a-chip biosensing and Raman

spectroscopy [11]–[14]. Despite this research area reaching its maturity and entering the commercialization stage, there remains the important bottleneck of efficiently and reliably connecting micro- and nanoscale on-chip devices to optical fibers [15], preferably single-mode fibers (SMF), to avoid complex interference processes. The waveguide core is usually less than 1 μm to prevent higher-order modes propagation, while the core dimensions of SMFs are not less than a few micrometers for free-space wavelengths, λ , of 785 and 1550 nm. Owing to high mode mismatching, this connection is accompanied by high coupling losses [16] and high background noise [17]. High coupling loss affects all on-chip integrated devices and optical circuits. However, high background noise extremely affects Raman on-chip spectroscopy (due to the weak nature of the Raman signal) [14], [18] and other on-chip sensing devices because they are open structures. In addition, the propagation of the background radiation into the optical circuit may lead to an increase in fluorescence signals from the substrate and to interference between background radiation and the working mode of the waveguide [19]. Altogether, it leads to a decreased signal-to-noise ratio and a complication in the detection of the useful signal from the sample, and the necessity to fabricate additional filters on a chip. As a result, there is a need to develop a platform with a minimum level of background optical noises in addition to the task of increasing the coupling efficiency.

To increase the coupling efficiency, different techniques have been proposed such as in-plane tapered coupling [20]–[23], out-plane grating coupling [24], and usage of fiber lenses [25]. Nowadays, the use of tapered coupling schemes and grating couplers is one of the most popular techniques. However, these techniques have several drawbacks, one of which is that it is necessary to use relatively long coupling areas (up to 1 mm); and another is the relatively high background noise sometimes connected with them. All this is unsuitable and cumbersome in most cases. Despite significant research efforts endeavored to tackle the underlined challenges [26]–[33], this goal has yet to complete. Another promising approach is the use of tapered nanofibers produced using the hydrogen/oxygen flame brushing technique [34], [35]. Optical nanofibers can be produced with tip diameters up to 400–500 nm and with a 98.7% preservation of the initial light energy. Nevertheless, despite of the high mode matching of tapered nanofibers to on-chip waveguides and the ability to locally excite the waveguide, the alignment and mechanical stabilization of the fiber tip with the chip in front of the waveguide with high precision is still an open problem.

Recently, simple photoplastic connectors have been proposed that allow the efficient connection of an SMF to metal-insulator-metal plasmon waveguides [36]. Inspired by this idea, we modified the connector and in the present paper propose a single-mode waveguides platform for on-chip integrated photonics. Usage of this platform allows one to connect a tapered optical fiber or fiber lens to on-chip waveguides with high alignment precision and to mechanically fix the fiber to the chip to prevent defocusing, lateral shift and angular detuning during the operation of the device. The metal screen of the connector made of gold prevents the penetration of background radiation into the optical circuit. Reconciliation of the optical fiber with on-chip waveguides is realized through mode transformation in the connector. This transformation is a resonance process, i.e., it is performed with the help of wave re-reflection. Consequently, to achieve maximum bandwidth and minimum losses, it is necessary to reduce the re-reflection. To achieve this aim, we performed impedance-matching analysis based on the transmission line theory and numerically optimized the whole platform consisting of the tapered nanofiber, the connector and Si/Si₃N₄ waveguides on a SiO₂ substrate. Si₃N₄ and Si waveguides with free-space wavelengths of 785 nm (frequency $f = 382.2$ THz) and 1550 nm ($f = 193.5$ THz), respectively were analyzed. The alignment tolerance and laser wavelength drift were also analyzed. Numerical analysis was performed using the three-dimensional finite integration technique [37] in the time domain. The Drude model was used to describe the interaction of the metals with electromagnetic radiation. The parameters of the materials used can be found in the Supplementary materials S1. The convergence of the numerical simulation results and the mesh adaptation of the models used had been analyzed before the simulation (see S2).

2. General Concept of the Platform

The spatial geometry of the platform is shown in Fig. 1. The platform consists of a SiO₂ substrate (red color), tapered nanofiber (cyan color), Si or Si₃N₄ waveguides (blue color), and the connector.

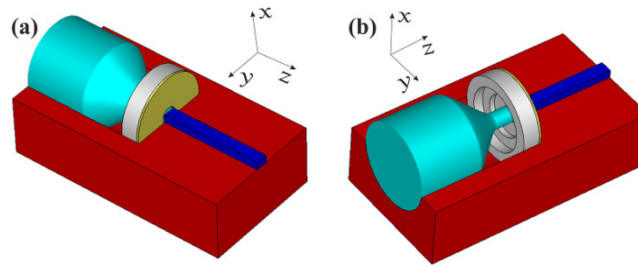


Fig. 1. Spatial geometry of the platform: (a) front view, (b) back view.

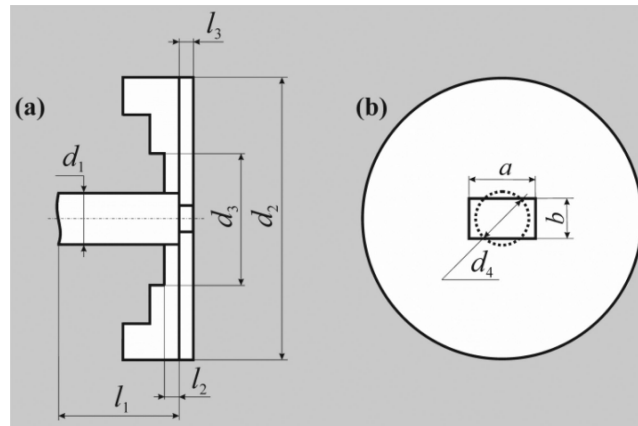


Fig. 2. Schematic illustration of the connector: (a) cross-sectional view, (b) view from the hole. d_1 is the diameter of the nanofiber tip and, correspondingly, the diameter of the first section of the SU-8 substrate (thickness of the first section is equal to 0); d_2 is the diameter of the Au screen and, correspondingly, the diameter of the fourth section of the SU-8 substrate; d_3 is the diameter of the third section of the SU-8 substrate; d_4 is the diameter of the circular hole in the Au screen; a and b are the width and height of the rectangular hole, respectively; l_1 is the length of the nanofiber tip; l_2 is the thickness of the second section of the SU-8 substrate; l_3 is the thickness of the Au screen.

As an example of Si/Si₃N₄ waveguide, we chose the strip waveguide. The tapered fiber and the connector are in a half groove that can be realized in a circular, rectangular, trapezoidal, or triangular shape made in the SiO₂ substrate. The connector consists of an Au screen (gold color) and SU-8 substrate (silver color). The SU-8 substrate contains 4 sections for mechanical strength. There is a hole of rectangular or circular shape in the Au screen. This rectangular (RH) or circular (CH) hole serves to electromagnetically connect the fiber and the waveguide.

A schematic illustration of the connector with its legend is given in Fig. 2.

The rectangular and circular holes in the Au screen can be considered as rectangular and circular metal waveguides, respectively. Conversely, the considered structure is highly symmetric. Due to these facts, the operating principle of the platform is as follows: for the RH, the strongly guided fundamental HE₁₁ mode of the nanofiber excites the fundamental TE₁₀ (polarized along x axis) or working TE₀₁ (polarized along y axis) modes, depending on the polarization direction. For the CH, the fundamental HE₁₁ mode excites the fundamental TE₁₁ mode polarized in either the x or y direction. In its turn, the fundamental TE₁₀ or the fundamental TE₁₁ polarized in the x direction excites the quasi-TM₀ mode of the Si₃N₄/Si waveguide, while the working TE₀₁ or fundamental TE₁₁ polarized in the y direction excites the quasi-TE₀ mode of the Si₃N₄/Si waveguide. Therefore, the excitation of the quasi-TM₀ and quasi-TE₀ mode can be controlled by the polarization of the fundamental HE₁₁ mode of the fiber. A more detailed analysis of the propagation of the modes will be provided in the next section.

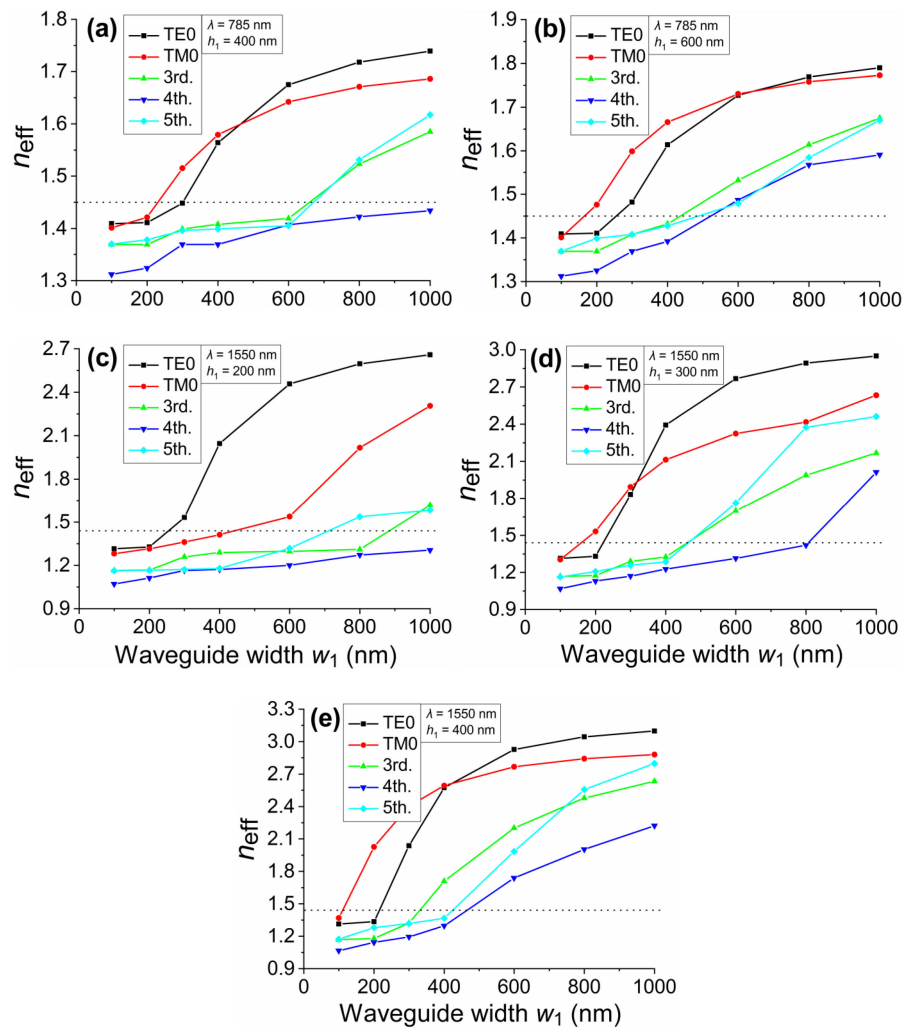


Fig. 3. Dependence of the effective refractive index n_{eff} for first five modes on the waveguide width w_1 at a waveguide height h_1 of (a) 400 nm and (b) 600 nm for $\lambda = 785$ nm, and a h_1 of (c) 200 nm, (d) 300 nm and (e) 400 nm for $\lambda = 1550$ nm; the black dotted lines show the silica line.

3. Results and Discussion

3.1 Analysis of the Appropriate Sizes of the Si_3N_4 and Si Waveguides on SiO_2 Substrate to Achieve Single-Mode Regime

First of all, we need to choose such sizes of the Si_3N_4 (for $\lambda = 785$ nm) and Si (for $\lambda = 1550$ nm) waveguides that allow the propagation of the working TE_0 or TM_0 modes only. To this end, we performed effective refractive index analysis [38]. Detailed description of the model used for the simulation can be found in S2, model 1. Fig. 3 shows the dependence of the effective refractive index n_{eff} for the first five modes on the waveguide width, w_1 at a waveguide height, h_1 of (a) 400 nm and (b) 600 nm for $\lambda = 785$ nm, and a h_1 of (c) 200 nm, (d) 300 nm and (e) 400 nm for $\lambda = 1550$ nm. It should be noted here that we are not interested in the classification of the modes, except the first mode that is quasi- TE_0 and the second mode that is quasi- TM_0 mode (usually, for 2D waveguides, two indices are used such as $\text{TM}_{1,1}$, or just fundamental quasi- TE_0 and fundamental quasi- TM_0 mode without indices).

For $\lambda = 785$ nm in Figs. 3(a) and 3(b), it is clear that the single-mode regime (TE_0 or TM_0 mode propagating) is achievable at $w_1 = 600$ nm and $h_1 = 400$ nm. For $\lambda = 1550$ nm in Figs. 3(c–e), it is

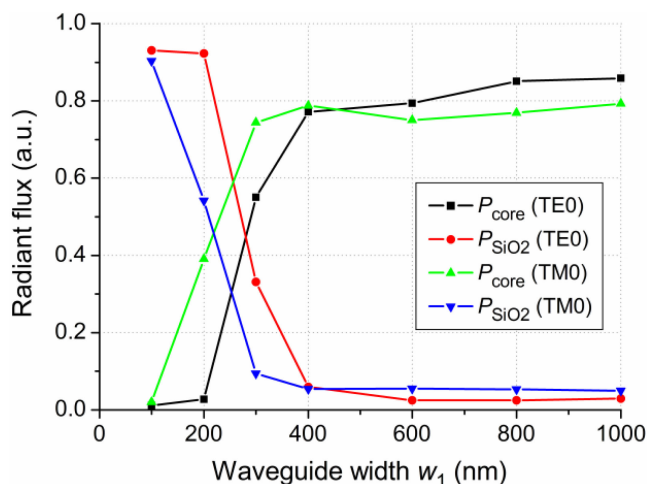


Fig. 4. Dependence of the radiant flux, P_{core} of the TE_0 or TM_0 modes through the waveguide core and close surroundings, and the radiant flux, P_{SiO_2} of the TE_0 or TM_0 modes through the SiO_2 substrate on the waveguide width w_1 for $\lambda = 785$ nm ($h_1 = 400$ nm); a.u., arbitrary units.

evident that the single-mode regime (TE_0 or TM_0 mode propagating) is achievable either at $w_1 = 400$ nm and $h_1 = 300$ nm, or at $w_1 = 600$ nm and $h_1 = 200$ nm. However, in the case of $w_1 = 600$ nm and $h_1 = 200$ nm, the value of n_{eff} for the TM_0 mode is only slightly higher than the value of the silica refractive index (see Fig. 3(c)). This can lead to a weak TM_0 mode excitation in the Si waveguide. Therefore, for further analysis, we chose $w_1 = 400$ nm and $h_1 = 300$ nm for $\lambda = 1550$ nm.

Besides, due to the light wave diffraction limit [38], it is important to know which part of the overall energy of the working mode (TE_0 or TM_0) will propagate in the waveguide core and close surroundings at the chosen waveguide height, h_1 . Fig. 4 illustrates the dependence of the radiant flux, P_{core} of the TE_0 and TM_0 modes through the waveguide core and close surroundings, and the radiant flux, P_{SiO_2} of the TE_0 and TM_0 modes through the SiO_2 substrate on the waveguide width, w_1 for $\lambda = 785$ nm ($h_1 = 400$ nm). The flux of the radiation shows a power fraction of certain modes in certain areas of the waveguide.

Note that the radiant flux, P_{core} displays the flux of the radiation without considering the energy reflection from the end of the waveguide (reflectance $\approx 12.5\%$, so the real radiant flux, P_{core} is slightly higher). Fig. 4 illustrates that at $w_1 = 600$ nm and $h_1 = 400$ nm, most of the mode energy propagates in the core and close surroundings and only a small fraction of the energy (almost equal to 0) propagates in the SiO_2 substrate.

3.2 Crucial Dimensions of the Tapered Fiber

In [35], it was shown that the cutoff value at which only the fundamental HE_{11} mode of the nanofiber can propagate is wavelength-dependent and corresponds to $d/\lambda \approx 0.73$ for a refractive index, n of silica = 1.45. For $\lambda = 785$ nm, it corresponds to 573 nm and for $\lambda = 1550$ nm, the value is 1131 nm. At the same time, the diameter of the nanofiber should not be less than 470 and 1030 nm for a λ of 785 and 1550 nm, respectively, so as to preserve most of the initial SMF energy (up to 99%). Therefore, the working single-mode range for the tapered optical fiber is 570–470 and 1130–1030 nm for a wavelength of 785 and 1550 nm, respectively.

3.3 Analysis of the Transformation Efficiency of the Tapered Optical Fiber Mode to the On-Chip Waveguide Mode and Optimization of the Platform

The entire platform, as a transmission line, can be divided into four transmission line segments: the tapered fiber; the fiber covered by the second section of the SU-8 substrate; the hole (RH or CH)

in the Au screen; and the Si₃N₄ or Si waveguide on the SiO₂ substrate. The second segment can be neglected if the thickness, l_2 is very small compared to the free-space wavelength, λ ($l_2 \leq \lambda/4$; for example, if $l_2 < 195$ nm for $\lambda = 785$ nm). During the analysis, we set $l_2 = 100$ nm and neglected line 2. Therefore, the task of impedance-matching is required only for the remaining three line segments. To accomplish this task, we combined analytical derivations based on the transmission line theory and numerical simulations.

Analytically, for an input Z_{in} , characteristic impedance, Z_0 and load impedance, Z_l for a transmission line without losses, we can write the following equation [39]:

$$\frac{Z_l}{Z_0} = \left[\frac{Z_{in}}{Z_0} + i \tan(\beta l) \right] / \left[1 + i \frac{Z_{in}}{Z_0} \tan(\beta l) \right], \quad (1)$$

where β is a propagation constant for the line, l is the length of the line and i is the imaginary unit. For our cascade, we can set $Z_{in} = Z_0$ for the tapered fiber, $Z_l = Z_0$ for the Si₃N₄ or Si waveguide, and $Z_0 = Z_0$ for the hole in the Au screen (Z_0 is the characteristic impedance of a segment). When $Z_l = Z_0$ in (1), Z_{in} is also equal to Z_0 , and we will obtain an ideally matched line with zero reflection. Thus, in our case, we must match three values of Z_0 (for the Si₃N₄/Si waveguide, the hole in the Au screen, and the tapered fiber) to obtain minimum reflectance at each segment interface and maximum transmission through the line.

3.3.1 Characteristic Impedances of Si₃N₄ and Si Waveguides: For the Si₃N₄ waveguide ($\lambda = 785$ nm, $w_1 = 600$ nm, $h_1 = 400$ nm), the transmission line theory [40] gives $Z_0(\text{TE}_0) = 175.04 \Omega$ and $Z_0(\text{TM}_0) = 215.87 \Omega$. For the Si waveguide ($\lambda = 1550$ nm, $w_1 = 400$ nm, $h_1 = 300$ nm), the theory gives $Z_0(\text{TE}_0) = 60.39 \Omega$ and $Z_0(\text{TM}_0) = 171.68 \Omega$.

3.3.2 Case of a Rectangular Hole (RH): The rectangular hole in the Au screen can be considered as a rectangular metal waveguide with dimensions $a \times b$, where a represents the wide wall and b represents the narrow wall (see Fig. 2(b)). To excite the TE₀ mode in the Si₃N₄/Si waveguide, it is necessary to excite the TE₀₁ mode in the RH. To excite the TM₀ mode in the Si₃N₄/Si waveguide, it is necessary to excite the TE₁₀ mode in the RH. To satisfy the characteristic impedance, Z_0 of the Si₃N₄/Si for the TE₀ and TM₀ modes, respectively, we calculated the appropriate dimensions, a and b for the RH for the TE₀₁ and TE₁₀ modes.

For the TE₁₀ mode, one can mathematically express a via b in the following form [40]:

$$a = \sqrt{\lambda^2 + \frac{754^2}{Z_0^2(\text{TM}_0)} b^2} / 2. \quad (2)$$

Due to the nature of the electric field distribution for the TM₀ mode in the Si₃N₄/Si waveguide (direction along b), we expressed a through b .

For the TE₀₁ mode, one can mathematically express b through a in the following form:

$$b = \sqrt{\lambda^2 + \frac{754^2}{Z_0^2(\text{TE}_0)} a^2} / 2. \quad (3)$$

Due to the nature of the electric field distribution for the TE₀ mode in the Si₃N₄/Si waveguide (direction along a), we expressed b through a .

3.3.2.1 TE₁₀ Mode ($\lambda = 785$ nm): Let $b = h_1 = 400$ nm (height of the Si₃N₄ waveguide). Substituting $Z_0(\text{TM}_0) = 215.87 \Omega$ and $\lambda = 785$ nm into (2), we obtain $a = 801.28$ nm ≈ 800 nm. Note that these derivations were obtained for a perfect metal (PEC). For real lossy metals, it can be different due to plasmon mode excitation on the surface of the RH [41], [42]. This difference depends on the thickness of the surrounding metal (Au screen diameter d_2), and the thickness of l_3 for the RH. To confirm this, we performed numerical simulation for the real Au and found the dimensions, a and b that satisfies the impedance-matching condition $\{Z_0(\text{TE}_{10}) = Z_0(\text{TM}_0)\}$ to be equal to 750 and 400 nm, respectively. For this simulation, we took an Au screen with diameter, $d_2 = 4,000$ nm and thickness, $l_3 = 4,000$ nm. It should be noted that this effect will be negligible for l_3 that is small and d_2 that is large compared to the free-space wavelength and transverse sizes, a and b , respectively. However, it is better to set $a = 750$ nm, not 800 nm, to prevent the

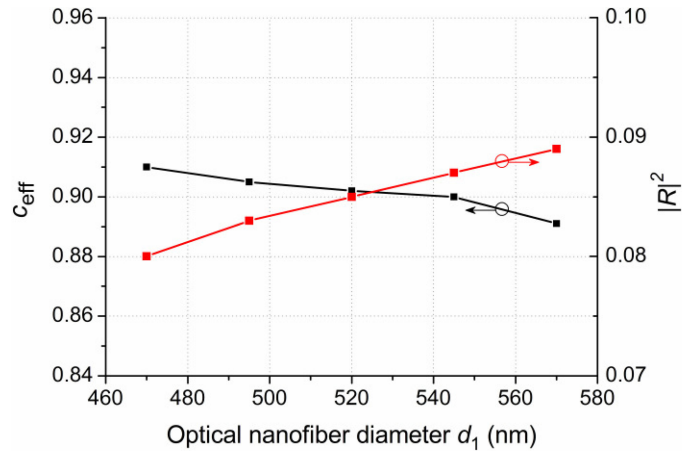


Fig. 5. Dependence of the power transformation efficiency, c_{eff} and power reflection coefficient, $|R|^2$ on the fiber diameter d_1 for the rectangular hole: $a = 750$ nm, $b = 400$ nm, $l_1 = 1,100$ nm, $l_2 = 100$ nm, $l_3 = 50$ nm, $d_2 = 4,000$ nm; $\lambda = 785$ nm.

propagation of high-order TE_{20} mode $\{\lambda_c(\text{TE}_{20}) = a; \lambda = 785$ nm $\}$. To confirm the applicability of the numerical simulation, we numerically found $Z_0(\text{TE}_{10})^{\text{PEC_numerical}}$ using the waveguide wavelength λ_w for PEC RH waveguide with $d_2 = 4,000$ nm and length, $l_3 = 4,000$ nm, and compared it with the $Z_0(\text{TE}_{10})^{\text{PEC_theory}}$ obtained using analytical derivations. The relative error is approximately 0.1%, thereby proving the applicability and accuracy of the combined analytical derivations and numerical simulations.

Figure 5 illustrates the dependence of the power transformation efficiency, c_{eff} and power reflection coefficient, $|R|^2$ at the point of radiant flux measurement on the fiber diameter, d_1 for an Au screen thickness, $l_3 = 50$ nm. Power transformation efficiency c_{eff} shows the amount of energy transformed from the optical fiber fundamental mode to on-chip waveguide fundamental mode, and it was the objective function of our optimization process (details of c_{eff} and $|R|^2$ calculations can be found in S3). A detailed description of the model used for simulation can be found in S2, model 2.

From Fig. 5, it is obvious that for the RH, it is possible to achieve c_{eff} as high as 91%. An Au screen thickness of 50 nm is enough for any background blocking because the skin-depth of gold is approximately 25 and 23 nm for $\lambda = 785$ and 1550 nm [43], respectively. Note that the numerical data in Fig. 5 were obtained with high accuracy (relative errors, $\delta \leq 0.16\%$ for the radiant flux and $\leq 0.1\%$ for S1,1 parameter; see S2).

Figure 6 shows the dependence of the c_{eff} on the Au thickness, l_3 for $d_1 = 570$ nm (calculated mode field diameter is 718.5 nm). In this case, the numerical data were obtained with normal accuracy (relative errors, $\delta \leq 4.2\%$ for the radiant flux and $\leq 3.6\%$ for S1,1 parameter; see S2) just to show the dependence qualitatively and to reduce the simulation time. The expediency of such an approach will be proved below in the case of the circular hole (see subsection 3.3.3.a, Figure 8 and the description of the Figure).

From Fig. 6, it is clear that the RH exhibits Fabry-Perot resonator-like behavior with a distance between two neighbor peaks of 403.9 nm ($\lambda/2 = 392.5$ nm, so relative error is approximately 3%—this falls within the accuracy range). The visibility (contrast) is equal to 0.146. Note that the thickness of the Au screen should be as small as possible to prevent high Ohmic losses and line mismatch due to increasing reactivity.

3.3.2.2 TE_{10} Mode ($\lambda = 1550$ nm): Let $b = h_1 = 300$ nm (height of the Si waveguide). Substituting $Z_0(\text{TM}_0) = 171.68 \Omega$ and $\lambda = 1550$ nm into (2), we obtain $a = 842.1$ nm ≈ 840 nm.

It should be noted that due to the much slower convergence of the results and the greater error of calculations at $\lambda = 1550$ nm compared to $\lambda = 785$ nm (see S2), the computational time increased significantly. As a result, we were forced to reduce the number of points analyzed at $\lambda = 1550$ nm.

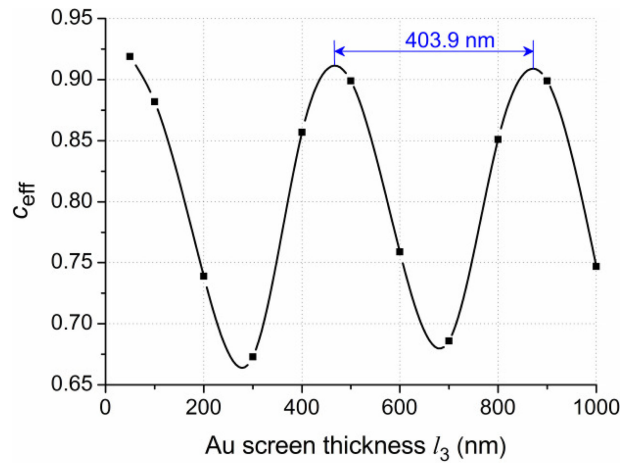


Fig. 6. Dependence of the power transformation efficiency, c_{eff} on the Au thickness, l_3 for the rectangular hole: $a = 750$ nm, $b = 400$ nm, $l_1 = 1,100$ nm, $l_2 = 100$ nm, $d_1 = 570$ nm, $d_2 = 4,000$ nm; $\lambda = 785$ nm.

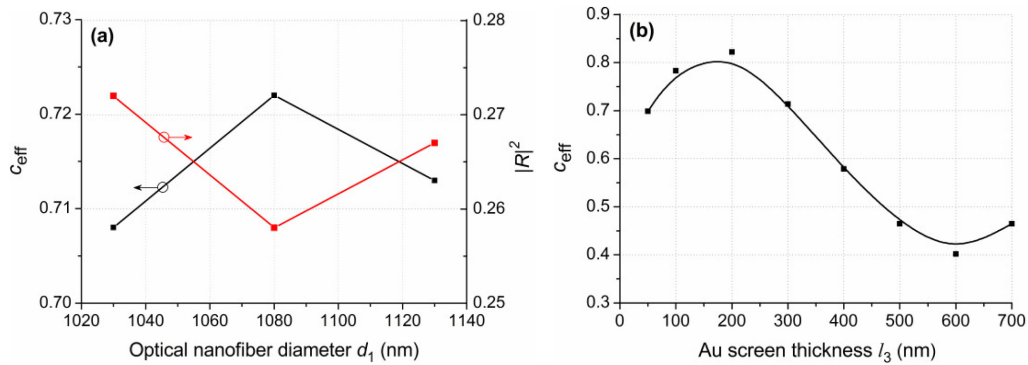


Fig. 7. Dependence of power transformation efficiency, c_{eff} and power reflection coefficient, $|R|^2$ on (a) the fiber diameter, d_1 for $l_3 = 50$ nm and (b) on the Au thickness l_3 for $d_1 = 1080$ nm for the rectangular hole: $a = 840$ nm, $b = 300$ nm, $l_1 = 1,100$ nm, $l_2 = 100$ nm, $d_2 = 4,000$ nm; $\lambda = 1550$ nm.

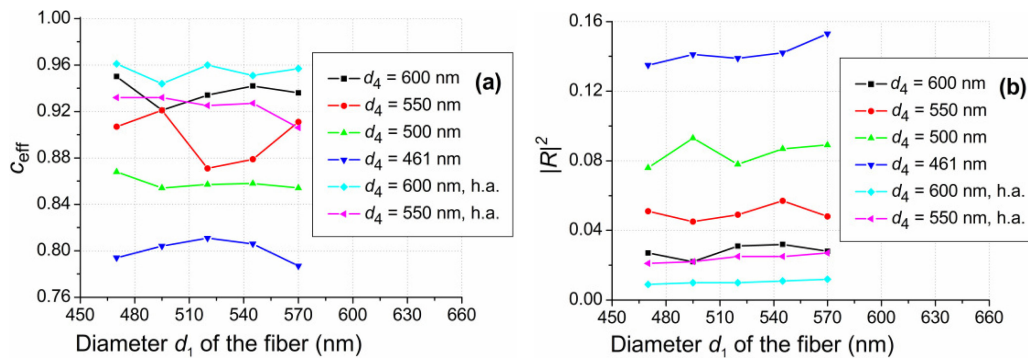


Fig. 8. Dependence of (a) power transformation efficiency c_{eff} and (b) power reflection coefficient $|R|^2$ for the TM_0 mode of the Si_3N_4 waveguide on the fiber diameter d_1 for the circular hole for different values of d_4 : $l_1 = 1,100$ nm, $l_2 = 100$ nm, $l_3 = 50$ nm, $d_2 = 4,000$ nm, $\lambda = 785$ nm; h.a., high accuracy.

TABLE 1
Values of Bessel Function Roots and λ_c for the Four First Modes of the Circular Waveguide

Mode type	p_{mn} or p'_{mn}	λ_c	λ_c , nm if $d_4 = 600$ nm ($\lambda = 785$ nm)	λ_c , nm if $d_4 = d_{\min} =$ 460.14 nm ($\lambda = 785$ nm)	λ_c , nm if $d = 1180$ nm ($\lambda = 1550$ nm)	λ_c , nm if $d_4 = d_{\min} = 908.56$ nm ($\lambda = 1550$ nm)
TE ₁₁	1.841	1.706d	1023.6	784.99	2013.08	1550.00
TM ₀₁	2.405	1.306d	783.6	600.94	1541.08	1186.58
TE ₂₁	3.050	1.028d	616.8	473.03	1213.04	933.99
TM ₁₁	3.832	0.820d	492.0	377.31	967.60	745.02

Figure 7 illustrates the dependence of the power transformation efficiency, c_{eff} and power reflection coefficient $|R|^2$ on (a) the fiber diameter, d_1 for an Au screen thickness, $l_3 = 50$ nm and (b) on an Au thickness, l_3 for $d_1 = 1080$ nm. From Fig. 7(b), it is obvious that for the RH, it is possible to achieve a c_{eff} as high as 82% at $l_3 \approx 200$ nm. The visibility (contrast) is equal to 0.343.

3.3.2.3 TE₀₁ Mode ($\lambda = 785$ nm): Let $a = w_1 = 600$ nm (width of the Si₃N₄ waveguide). Substituting $Z_0(\text{TE}_0) = 175.04 \Omega$ and $\lambda = 785$ nm into (3), we obtain $b = 1350.57$ nm ≈ 1350 nm. Therefore, analytical derivation gives $b > a$ —this cannot be satisfied. Due to the structural similarity of the TE₀₁ and TE₁₀ modes of rectangular metal waveguides to the TE₁₁ mode of circular metal waveguides, we will show, in the next subsection, the ability to excite the TE₀, as well as the TM₀ mode in the Si₃N₄/Si waveguide with a high power transformation efficiency, c_{eff} using circular holes in the Au screen.

3.3.2.4 TE₀₁ Mode ($\lambda = 1550$ nm): Let $a = w_1 = 400$ nm (width of the Si waveguide). Substituting $Z_0(\text{TE}_0) = 60.39 \Omega$ and $\lambda = 1550$ nm into (3), we obtain $b = 2614.8$ nm ≈ 2615 nm. Therefore, analytical derivation gives $b > a$ —this cannot be satisfied. This is similar to the TE₀₁ mode for $\lambda = 785$ nm.

3.3.3 Case of a Circular Hole (CH): For a circular metal waveguide of diameter d , the cutoff wavelength for the TE modes can be expressed as [38] $\lambda_c = \pi d/p_{mn}$, where p_{mn} is the n th root of the Bessel function of the first kind $J_m(p_{mn})$, i.e., n th root of the Eq. $J_m(p_{mn}) = 0$. Similarly, the cutoff wavelength for the TM modes can be expressed in the form $\lambda_c = \pi d/p'_{mn}$, where p'_{mn} is n th root of the Bessel function of the first kind $J_m(p'_{mn})$. In Table 1, the values of the Bessel function roots and λ_c for the four first modes of the circular waveguide are illustrated. If we use the free-space wavelength, λ instead of λ_c in the equation for the cutoff wavelength, we will obtain the minimal diameter d_{\min} at which the lowest TE₁₁ mode can propagate. These values are also indicated in Table 1.

From Table 1, it is obvious that the diameter, d_4 of the CH should be in the 600–461 nm and 1180–910 nm range for wavelengths of 785 and 1550 nm, respectively, to achieve the single-mode regime. Therefore, these ranges were chosen for further analysis.

Knowing the cutoff wavelength, we can calculate the wave impedance $Z_w(\text{TE}_{11})$ for the TE₁₁ mode for values of d_4 from the range of interest (600–461 nm and 1180–910 nm for wavelengths of 785 and 1550 nm, respectively). These values are shown in Table 2. From Table 2, it is evident that as d_4 approaches the value of the minimal diameter d_{\min} , the wave impedance grows rapidly (as it should).

3.3.3.1 Si₃N₄ Waveguide Excitation ($\lambda = 785$ nm): Fig. 8 shows the dependence of the (a) power transformation efficiency c_{eff} and (b) power reflection coefficient $|R|^2$ for the TM₀ mode of the Si₃N₄ waveguide on the fiber diameter d_1 for different values of d_4 . After comparing the values of c_{eff} and $|R|^2$ obtained at normal and high accuracies, it is obvious that to obtain qualitative dependencies, it is enough to use the simulation at normal accuracy, and to perform simulation at high accuracy for the curve of interest to obtain the exact value of the necessary parameter. The

TABLE 2
 Wave Impedance Values for the TE₁₁ Mode

d_4 , nm	$Z_w(\text{TE}_{11})$, Ω	
	$\lambda = 785$ nm	$\lambda = 1550$ nm
600	1,223.19	–
550	1,433.05	–
500	2,006.35	–
461	12,862.64	–
1180	–	2,429.14
1080	–	2,867.00
980	–	4,135.38
910	–	27,544.28

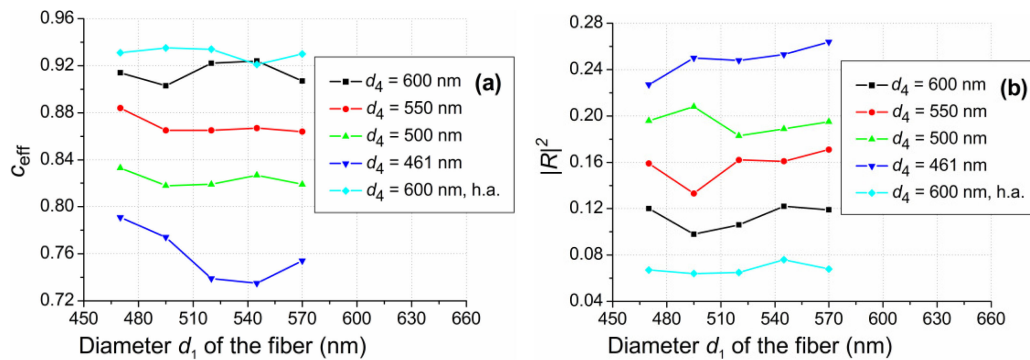


Fig. 9. Dependence of the (a) power transformation efficiency, c_{eff} and (b) power reflection coefficient, $|R|^2$ for the TE₀ mode of the Si₃N₄ waveguide on the fiber diameter, d_1 for the circular hole for different values of d_4 : $l_1 = 1,100$ nm, $l_2 = 100$ nm, $l_3 = 50$ nm, $d_2 = 4,000$ nm, $\lambda = 785$ nm; h.a., high accuracy.

c_{eff} is equal to 0.957 and 0.960 for $d_1 = 570$ and 520 nm, respectively, and for $d_4 = 600$ nm and a reflectance of approximately 1%. The c_{eff} decreases with decreasing d_4 due to increasing wave impedance for the TE₁₁ mode, leading to growing impedance mismatch.

Figure 9 shows the dependence of the (a) power transformation efficiency, c_{eff} and (b) power reflection coefficient, $|R|^2$ for the TE₀ mode of the Si₃N₄ waveguide on the fiber diameter, d_1 for different values of d_4 . The c_{eff} is equal to 0.930 and 0.934 for $d_1 = 570$ and 520 nm, respectively, and for $d_4 = 600$ nm and a reflectance of approximately 7%. In this case, the c_{eff} also decreases with decreasing d_4 due to increasing wave impedance for the TE₁₁ mode, leading to increasing impedance mismatch. However, the impedance mismatch is higher in this case than for the TM₀ mode (reflectance is higher) due to the fact that $Z_0(\text{TE}_0) = 175.04 \Omega < Z_0(\text{TM}_0) = 215.87 \Omega$.

Figure 10 shows the dependence of the c_{eff} on the thickness, l_3 of the Au screen for $d_4 = 600$ nm and $d_1 = 570$ nm. From Fig. 10, it is clear that the circular hole also exhibits Fabry-Perot resonator-like behavior. The visibility (contrast) is equal to 0.533 and 0.604 for the TM₀ and TE₀ modes, respectively. Consequently, the CH circular waveguide behaves more like a high-Q resonator compared to the rectangular one, and it is important to optimize it carefully before production.

3.3.3.2 Si Waveguide Excitation ($\lambda = 1550$ nm): Figure 11 illustrates the dependence of the (a) power transformation efficiency, c_{eff} and (b) power reflection coefficient, $|R|^2$ for the TM₀ mode of the Si waveguide on the fiber diameter, d_1 for different values of d_4 . The efficiency, c_{eff} is equal to 0.951 and 0.955 for $d_1 = 1,130$ and 1,030 nm, respectively, and for $d_4 = 1,180$ nm and a reflectance

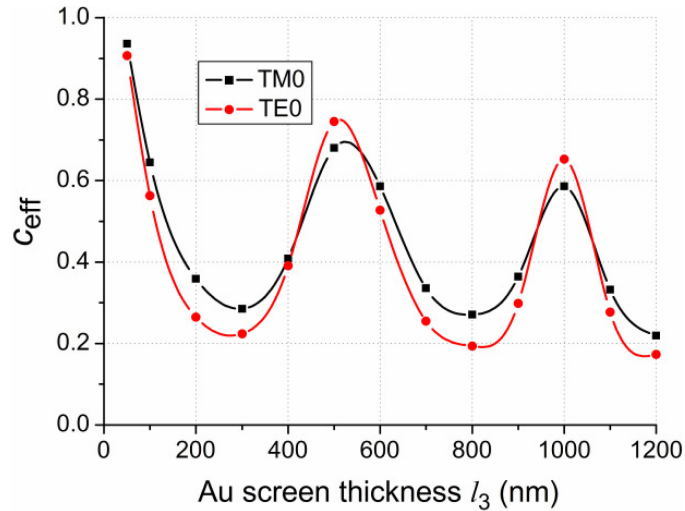


Fig. 10. Dependence of the power transformation efficiency, c_{eff} on the Au screen thickness, l_3 for the circular hole: $l_1 = 1,100$ nm, $l_2 = 100$ nm, $d_1 = 570$ nm, $d_2 = 4,000$ nm; $d_4 = 600$ nm, $\lambda = 785$ nm.

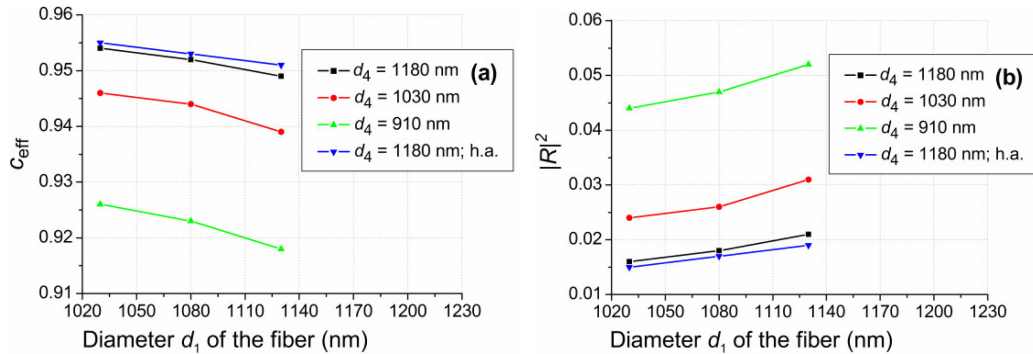


Fig. 11. Dependence of the (a) power transformation efficiency, c_{eff} and (b) power reflection coefficient, $|R|^2$ for the TM_0 mode of the Si waveguide on the fiber diameter d_1 for the circular hole for different values of d_4 : $l_1 = 1,100$ nm, $l_2 = 100$ nm, $l_3 = 50$ nm, $d_2 = 4,000$ nm, $\lambda = 1550$ nm; h.a., high accuracy.

of approximately 2%. The efficiency, c_{eff} decreases with decreasing d_4 due to increasing wave impedance for the TE_{11} mode that leads to increasing impedance mismatch.

Figure 12 shows the dependence of the (a) power transformation efficiency, c_{eff} and (b) power reflection coefficient, $|R|^2$ for the TE_0 mode of the Si waveguide on the fiber diameter, d_1 for different values of d_4 . The c_{eff} is equal to 0.901 for both $d_1 = 1,130$ and 1,030 nm and for $d_4 = 1,180$ nm and a reflectance of approximately 8%. In this case, the c_{eff} also decreases with decreasing d_4 due to increasing wave impedance for the TE_{11} mode, consequently leading to growing impedance mismatch. However, in this case, the impedance mismatch is higher than for the TM_0 mode (reflectance is higher) due to the fact that $Z_0(\text{TE}_0) = 60.39 \Omega < Z_0(\text{TM}_0) = 171.68 \Omega$.

Figure 13 illustrates the dependence of the c_{eff} on the thickness, l_3 of the Au screen for $d_4 = 1,030$ nm and $d_1 = 1,080$ nm. The visibility (contrast) is equal to 0.354 and 0.429 for the TM_0 and TE_0 modes, respectively.

3.4 Analysis of the Platform Bandwidth and Laser Wavelength Drift

To prove the high efficiency of the platform under laser wavelength drift from the central value, we performed bandwidth and wavelength drift analyses. As a working value, we chose 785 nm

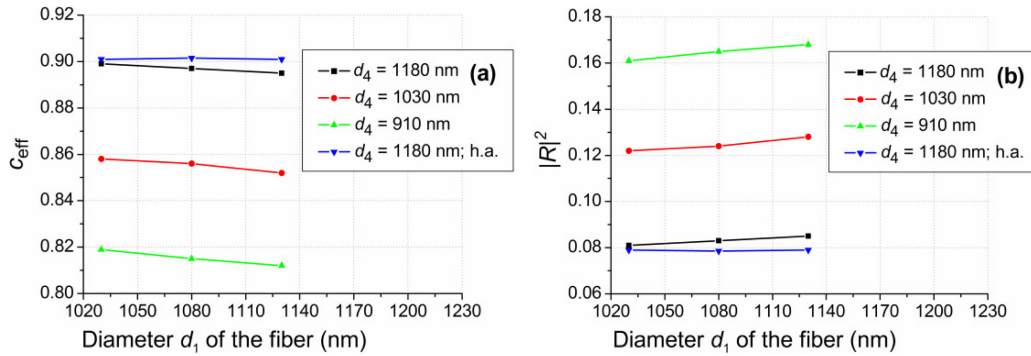


Fig. 12. Dependence of the (a) power transformation efficiency, c_{eff} and (b) power reflection coefficient, $|R|^2$ for the TE_0 mode of the Si waveguide on the fiber diameter, d_1 for the circular hole for different values of d_4 : $l_1 = 1,100$ nm, $l_2 = 100$ nm, $l_3 = 50$ nm, $d_2 = 4,000$ nm, $\lambda = 1550$ nm; h.a., high accuracy.

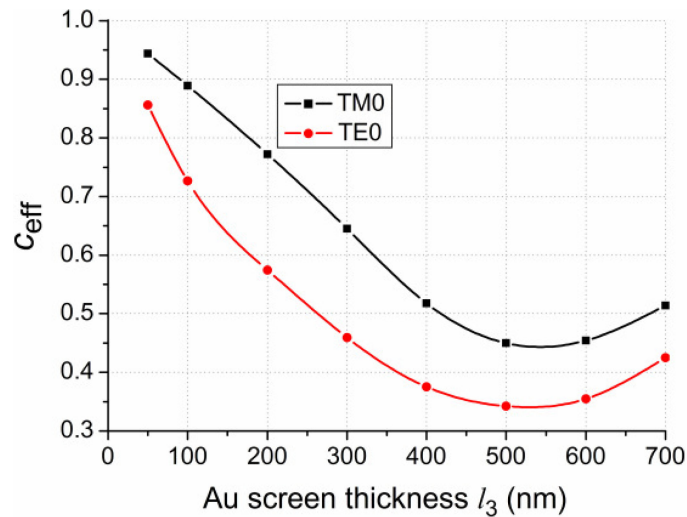


Fig. 13. Dependence of the power transformation efficiency, c_{eff} on the Au screen thickness, l_3 for the circular hole: $l_1 = 1,100$ nm, $l_2 = 100$ nm, $d_1 = 1,080$ nm, $d_2 = 4,000$ nm; $d_4 = 1,030$ nm, $\lambda = 1550$ nm.

and took a range from 549.5 to 1020.5 nm (for bandwidth analysis) and of ± 2 nm (785 ± 2 nm) (for laser drift analysis). In fact, the optical spectrum range is within 1 nm and 2 nm for modern off-chip [44] and on-chip [45] laser systems, respectively. At the same time, wavelength stability is within a range of ± 0.1 nm. Fig. 14 shows the dependence of (a) the c_{eff} in the wavelength range of 549.5-1020.5 nm and (b) the c_{eff} and $|R|^2$ in the wavelength range of 785 ± 2 nm for the TM_0 mode of the Si_3N_4 waveguide on the working wavelength for $d_1 = 570$ nm and $d_4 = 600$ nm. From Fig. 14(a), the platform bandwidth (power transformation efficiency $\geq 80\%$) is about 151 nm. At the same time, transformation efficiency is higher than 70% in the whole wavelength range from 549.5 to 1020.5 nm. This relatively wide wavelength range can be attributed to the previously performed optimization of the platform. However, small fluctuations of c_{eff} indicate that ideal matching between optical waveguides was not achieved. From Fig. 14(b), it is evident that the laser wavelength drift in the ± 2 nm range does not lead to significant changes in the c_{eff} (reduction less than 1%), and it proves the wavelength stability of the platform.

3.5 Alignment Tolerance Analysis

To prove the stability of the platform to technological drawbacks in manufacturing and the movement of the connector relative to the $\text{Si}_3\text{N}_4/\text{Si}$ waveguide during the operation of the device, we performed

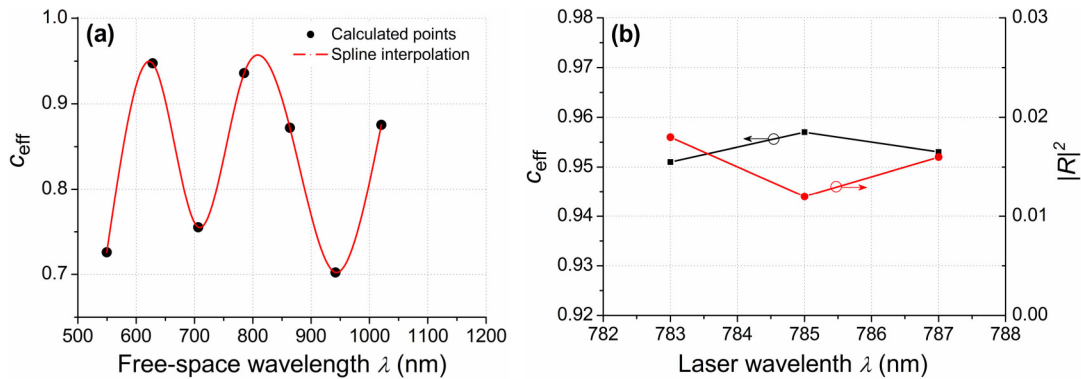


Fig. 14. Dependence of (a) the power transformation efficiency, c_{eff} in the range of 549.5-1020.5 nm and (b) the c_{eff} and power reflection coefficient, $|R|^2$ in the range of 785 ± 2 nm for the TM_0 mode of the Si_3N_4 waveguide on the working wavelength for the circular hole: $l_1 = 1,100$ nm, $l_2 = 100$ nm, $l_3 = 50$ nm, $d_1 = 570$ nm, $d_2 = 4,000$ nm, $d_4 = 600$ nm.

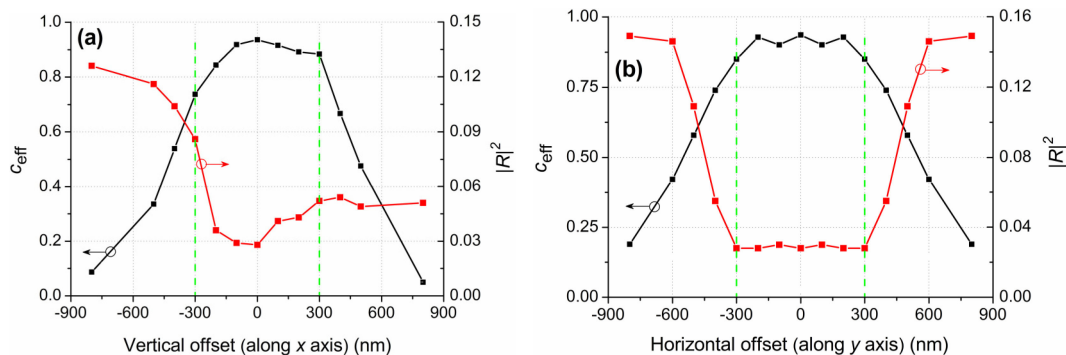


Fig. 15. Dependence of the power transformation efficiency c_{eff} and reflection coefficient $|R|^2$ for the TM_0 mode of the Si_3N_4 waveguide on the (a) vertical (along the x axis) and (b) horizontal (along the y axis) offset for the circular hole: $l_1 = 1,100$ nm, $l_2 = 100$ nm, $l_3 = 50$ nm, $d_1 = 570$ nm, $d_2 = 4,000$ nm, $d_4 = 600$ nm, $\lambda = 785$ nm; the green dashed lines represent the circular hole size.

alignment tolerance analysis. In Fig. 15, one can see the dependence of c_{eff} and $|R|^2$ on the lateral (a) vertical (movement of the waveguide along the x axis) and (b) horizontal (movement of the waveguide along the y axis) offset.

For the vertical offset (Fig. 15(a)), positive shift means the upward movement (in the positive direction along the x axis) of the Si_3N_4 waveguide on the substrate for a fixed fiber and connector. From Fig. 15(a), it is obvious that the efficiency, c_{eff} decreases faster when the waveguide moves downward. It can be attributed to the larger impedance mismatch between the CH and open space than that between the CH and the SiO_2 substrate (if we consider it as a waveguide). This effect is clearly seen in Fig. 15(a), where the power reflection coefficient, $|R|^2$ grows much faster with negative shifts and takes larger values (from 3 to 13%). In the case of positive shifts, the reflection coefficient grows less significantly and takes smaller values (from 3 to 5%). From Fig. 15(a), it is also evident that the vertical lateral alignment tolerance of the platform (transformation efficiency $\geq 80\%$) is within a range of -250 to 350 nm, i.e., approximately 600 nm. In the case of horizontal offset, the dependence is fully symmetric due to the full symmetry of the structure with respect to the plane, $y = 0$. From Fig. 15(b), the lateral horizontal alignment tolerance of the platform (transformation efficiency $\geq 80\%$) is observed to be within a range of -350 to 350 nm, i.e., approximately 700 nm.

In Fig. 16, one can see the dependence of c_{eff} and $|R|^2$ on the longitudinal offset (movement of the waveguide along the z-axis). From Fig. 16, it is clear that the longitudinal alignment tolerance for the platform (transformation efficiency $\geq 80\%$) is approximately 70 nm.

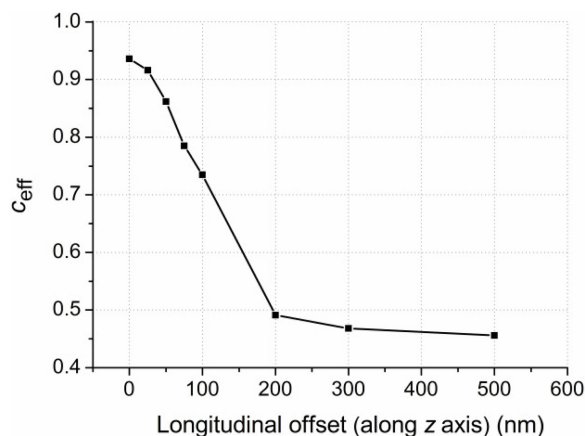


Fig. 16. Dependence of the power transformation efficiency, c_{eff} for the TM_0 mode of the Si_3N_4 waveguide on the longitudinal offset (along the z -axis) for the circular hole: $l_1 = 1,100$ nm, $l_2 = 100$ nm, $l_3 = 50$ nm, $d_1 = 570$ nm, $d_2 = 4,000$ nm, $d_4 = 600$ nm, $\lambda = 785$ nm.

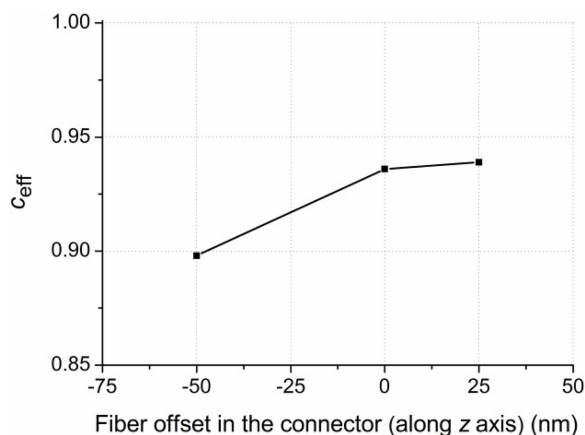


Fig. 17. Dependence of the power transformation efficiency, c_{eff} for the TM_0 mode of the Si_3N_4 waveguide on the longitudinal fiber offset (along the z -axis) in the connector for the circular hole: $l_1 = 1,100$ nm, $l_2 = 100$ nm, $l_3 = 50$ nm, $d_1 = 570$ nm, $d_2 = 4,000$ nm, $d_4 = 600$ nm, $\lambda = 785$ nm.

In the next step, we perform the analysis of the nanofiber offset in the connector along the z -axis, because in some cases, the diameter of the nanofiber, d_1 nm is smaller than the diameter of the circular hole, d_4 (for instance, $d_1 = 570$ nm and $d_4 = 600$ nm at $\lambda = 785$ nm). This may lead to a complexity of fiber fixing exactly in front of the Au screen (as schematically illustrated in Fig. 2(a)). The results of this analysis are shown in Fig. 17. From Fig. 17, we can conclude that the longitudinal fiber offset in the connector does not lead to a significant change in the c_{eff} (reduction less than 4.4%), and for the +25 nm offset (nanofiber enters the CH in the Au screen at 25 nm), it even leads to a slight increase in the c_{eff} (increased by 0.32%).

3.6 Electric Field Distribution and Power Flow

Figure 18 shows the electric field distribution (a, c) and the z -component of the time-averaged Poynting vector (b, d) for the waveguide excitation with (a, b) usual single-mode fiber with a core diameter of 2,000 nm (calculated mode field diameter is 2,128 nm), and (c, d) using the proposed platform. The case of quasi- TM_0 mode in the Si_3N_4 waveguide is illustrated ($\lambda = 785$ nm). From Figs. 18(a, b), it can be seen that for the usual SMF, there is a background radiation that propagates

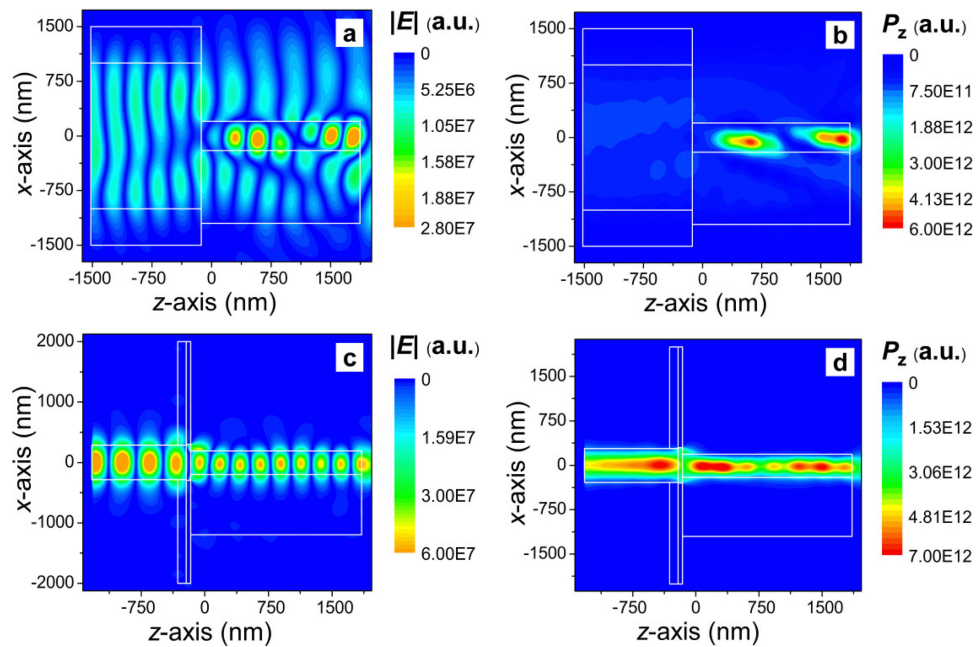


Fig. 18. (a), (c) Electric field distribution and (b), (d) z-component of the time-averaged Poynting vector for waveguide excitation with (a), (b) usual single-mode fiber with a core diameter of 2,000 nm and (c), (d) using the proposed platform; a.u., arbitrary units.

in the substrate and in the free-space far from the waveguide. In addition, due to the interference between the background and TM_0 modes, the electric field distribution in the Si_3N_4 waveguide is greatly distorted. For the platform in Figs. 18(c, d), the background is almost absent (see Fig. 18(d)), leading to virtually ideal electric field distribution for the TM_0 mode in the Si_3N_4 waveguide (see Fig. 18(c)). These results prove the background-noise-reduced working regime of the proposed platform.

4. Experimental Feasibility

Although the design of the platform is based on analytical and numerical analyses, we would like to discuss the experimental process on the basis of some experimental works. Details of the manufacturing of SOI and Si_3N_4 waveguides can be found elsewhere [46]–[49]. The half groove of different shapes in Si wafers can be produced by different lithographic and etching techniques [46], [50], [51]. The photoplastic connector is fabricated as follows [36] (see schematics in Fig. 19): (1) an oxide layer is produced on the Si wafer by thermal oxidation; (2) after deposition of a sacrificial layer, the gold screen is created using vacuum evaporation; (3) a photoresist is deposited on the Au screen; (4) a hole of the appropriate shape (rectangular or circular) and size is created in the Au screen through ultraviolet (UV) photolithography process; (5) the photoresist (SU-8) is deposited on the Au screen using a spin-coating procedure [52]; (6) the SU-8 portion is then exposed to UV radiation and developed to create a relief with 4 sections with multiple overlay exposure; (7) the tapered optical fiber is then inserted into section 1 of the SU-8 and fixed using UV glue; (8) the optical fiber in the connector is separated from the wafer. In this way, the proposed platform can be manufactured using commonly used and readily available fabrication techniques, which makes it very potential for the mass-manufacturing process. Due to the fact that the proposed platform has relatively high lateral and longitudinal tolerances, it offers the possibility of fabricating the proposed platform using described common fabrication techniques at high efficiency. At the same time, fabricated platform can be tested by different wafer-scale testing methods [53]–[55].

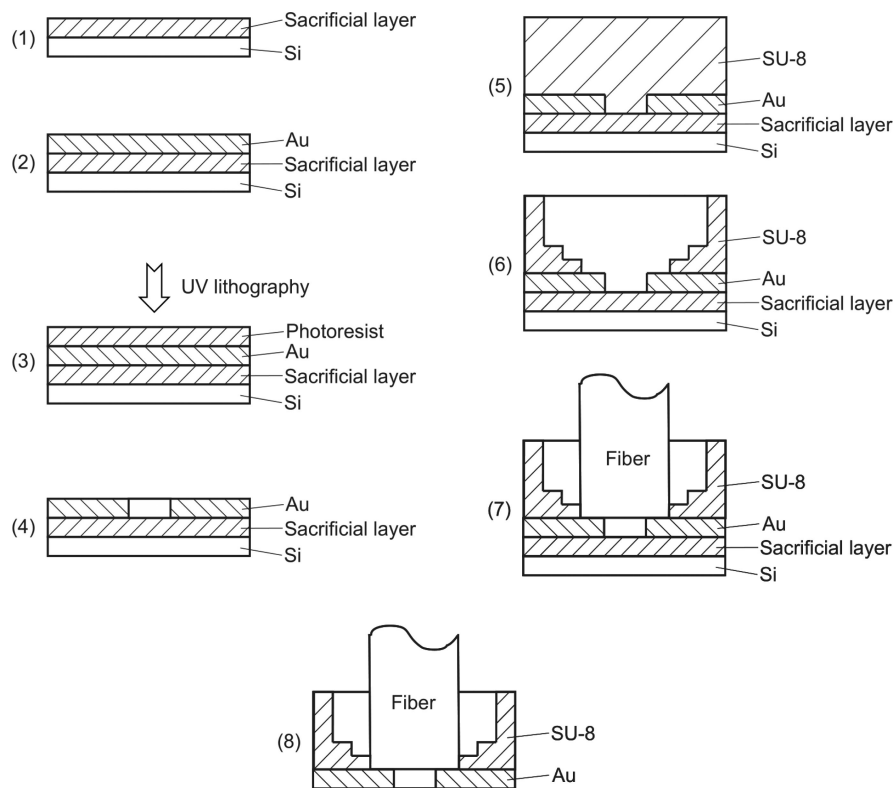


Fig. 19. Schematic illustration of the fabrication process of the connector.

5. Conclusion

In this work, we proposed a modified single-mode waveguides platform for on-chip integrated photonics that allows one to efficiently connect a tapered fiber or fiber lens to on-chip waveguides with high alignment precision and to mechanically fix the fiber to the chip. The main element of the modified platform is the connector that consists of an Au screen and an SU-8 substrate. There is a hole in the Au screen for the electromagnetic connection of the fundamental HE_{11} mode of a tapered optical nanofiber to the working quasi- TE_0 or quasi- TM_0 mode of a Si_3N_4/Si waveguide. Holes of rectangular (RH) and circular (CH) shapes were considered. We performed impedance-matching analysis and numerically optimized the platform, allowing us to achieve an optical tapered fiber mode to on-chip waveguide mode transformation efficiency as high as 96% (-0.177 dB) for both the TE_0 and TM_0 modes at wavelengths of 785 and 1550 nm in the case of the CH. For the RH, it was shown that efficient excitation is only possible for the TM_0 mode (91 and 82% at the wavelengths of 785 and 1550 nm, respectively). In this way, these results show much higher efficiency in comparison with that which was obtained in the previous work (83.7%, [36]). In addition, it was shown that using the previous design of the connector it is impossible to achieve high transformation efficiency for both quasi- TE_0 and quasi- TM_0 modes. At the same time, the current efficiency is higher or comparable with the best ones obtained by other groups using other structures, for instance, using adiabatic tapers (70.8% [20], 98.3% [22], and 80% [23]) or grating coupling (70.8%, [24], over 96% [31], 71% [32], 82% [33], 78% [56], and 84.53% [57]). It was also illustrated that metal screen of the connector made of gold prevents any penetration of background radiation into the optical circuit, something which it is not possible to achieve in all cases using tapers or grating couplers. The platform bandwidth (transformation efficiency $\geq 80\%$) is 151 nm. At the same time, transformation efficiency is higher than 70% in the wide wavelength range of 471 nm. Laser wavelength drift analysis showed that the transformation efficiency is stable (reduction less

than 1%) within an offset range of ± 2 nm, enough for modern on-chip and off-chip coherent light sources. The horizontal and vertical lateral alignment tolerances for the platform (transformation efficiency $\geq 80\%$) were 700 and 600 nm, respectively while the longitudinal alignment tolerance was approximately 70 nm. Due to the relatively high lateral and longitudinal tolerances, it is possible to produce the platform at high efficiency using existing nanotechnologies. According to the reciprocity principle, the connector may be also used to couple-out a waveguide mode. Therefore, we hope that this platform accelerates the realization of fully on-chip Raman spectroscopes and may be of practical importance in other on-chip integrated photonic devices.

References

- [1] Z. Zhou, B. Yin, and J. Michel, "On-chip light sources for silicon photonics," *Light Sci. Appl.*, vol. 4, 2015, Art. no. e358.
- [2] B. Lee, A. Biberman, J. Chan, and K. Bergman, "High-performance modulators and switches for silicon photonic networks-on-chip," *IEEE J. Sel. Topics Quantum Electron.*, vol. 16, no. 1, pp. 6–22, Jan./Feb. 2010.
- [3] D. Dai, "Silicon nanophotonic integrated devices for on-chip multiplexing and switching," *J. Lightw. Technol.*, vol. 35, no. 4, pp. 572–587, Feb. 2017.
- [4] S. Kocaman, M. Aras, N. Panoiu, M. Lu, and C. Wong, "On-chip optical filters with designable characteristics based on an interferometer with embedded silicon photonic structures," *Opt. Lett.*, vol. 37, pp. 665–667, 2012.
- [5] R. Baets *et al.*, "Silicon photonics: Silicon nitride versus silicon-on-insulator," in *Proc. Opt. Fiber Commun. Conf.*, Anaheim, CA, USA, 2016, Paper Th3J.1.
- [6] L. Zhang, Y. Yue, R. Beausoleil, and A. Willner, "Flattened dispersion in silicon slot waveguides," *Opt. Exp.*, vol. 18, pp. 20529–20534, 2010.
- [7] M. Roussey *et al.*, "Strip-loaded horizontal slot waveguide," *Opt. Lett.*, vol. 42, pp. 211–214, 2017.
- [8] M. Chamanzar, Z. Xia, S. Yegnanarayanan, and A. Adibi, "Hybrid integrated plasmonic-photonic waveguides for on-chip localized surface plasmon resonance (LSPR) sensing and spectroscopy," *Opt. Exp.*, vol. 21, pp. 32086–32098, 2013.
- [9] Y. Fainman, M. Nezhad, D. Tan, K. Ikeda, O. Bondarenko, and A. Grieco, "Silicon nanophotonic devices for chip-scale optical communication applications (Invited)," *Appl. Opt.*, vol. 52, pp. 613–624, 2013.
- [10] M. Forsell, "A scalable high-performance computing solution for networks on chips," *IEEE Micro*, vol. 22, no. 5, pp. 46–55, Sep./Oct. 2002.
- [11] A. F. Gavela, D. G. García, J. Ramirez, and L. Lechuga, "Last advances in silicon-based optical biosensors," *Sensors*, vol. 16, no. 3, 2016, Art. no. 285.
- [12] A. Subramanian *et al.*, "Silicon and silicon nitride photonic circuits for spectroscopic sensing on-a-chip (Invited)," *Photon. Res.*, vol. 3, pp. B47–B59, 2015.
- [13] B. Momeni, "Silicon nanophotonic devices for integrated sensing," *J. Nanophoton.*, vol. 3, 2009, Art. no. 031001.
- [14] A. Dhakal *et al.*, "Single mode waveguide platform for spontaneous and surface-enhanced on-chip Raman spectroscopy," *Interface Focus*, vol. 6, 2016, Art. no. 20160015.
- [15] S. Gröblacher, J. T. Hill, A. H. Safavi-Naeini, J. Chan, and O. Painter, "Highly efficient coupling from an optical fiber to a nanoscale silicon optomechanical cavity," *Appl. Phys. Lett.*, vol. 103, 2013, Art. no. 181104.
- [16] R. Orobtcchouk, "On chip optical waveguide interconnect: The problem of the in/out coupling," in *Optical Interconnects: The Silicon Approach*, L. Pavesi, G. Guillot, Eds., Berlin, Germany: Springer, 2006, pp. 263–290.
- [17] N. Kopeika and J. Bordogna, "Background noise in optical communication systems," *Proc. IEEE*, vol. 58, no. 10, pp. 1571–1577, Oct. 1970.
- [18] Q. Zheng, L. Huang, W. Li, Q. Feng, C. Fu, and J. Yu, "NSNI mitigation in bi-directional Raman amplified unrepeated system using split-DBP," *J. Lightw. Technol.*, vol. 36, no. 16, pp. 3494–3501, Aug. 2018.
- [19] Y. Morozov and A. Lapchuk, "Signal of microstrip scanning near-field optical microscope in far- and near-field zones," *Appl. Opt.*, vol. 55, pp. 3468–3477, 2016.
- [20] C. Liao, Y. Yang, S. Huang, and M. Lee, "Fiber-core-matched three-dimensional adiabatic tapered couplers for integrated photonic devices," *J. Lightw. Technol.*, vol. 29, no. 5, pp. 770–774, Mar. 2011.
- [21] A. Khilo, M. Popović, M. Araghchini, and F. Kärtner, "Efficient planar fiber-to-chip coupler based on two-stage adiabatic evolution," *Opt. Exp.*, vol. 18, pp. 15790–15806, 2010.
- [22] Y. Fu, T. Ye, W. Tang, and T. Chu, "Efficient adiabatic silicon-on-insulator waveguide taper," *Photon. Res.*, vol. 2, pp. A41–A44, 2014.
- [23] J. Liu *et al.*, "Double inverse nanotapers for efficient light coupling to integrated photonic devices," *Opt. Lett.*, vol. 43, pp. 3200–3203, 2018.
- [24] N. Na *et al.*, "Efficient broadband silicon-on-insulator grating coupler with low backreflection," *Opt. Lett.*, vol. 36, pp. 2101–2103, 2011.
- [25] H. Melkonyan, K. Sloyan, K. Twayana, P. Moreira, and M. Dahlem, "Efficient fiber-to-waveguide edge coupling using an optical fiber axicon lens fabricated by focused ion beam," *IEEE Photon. J.*, vol. 9, no. 4, Aug. 2017, Art. no. 7104309.
- [26] J. H. Song and X. Rottenberg, "Low-back-reflection grating couplers using asymmetric grating trenches," *IEEE Photon. Technol. Lett.*, vol. 29, no. 4, pp. 389–392, Feb. 2017.
- [27] D. Vermeulen *et al.*, "Reflectionless grating couplers for silicon-on-insulator photonic integrated circuits," *Opt. Exp.*, vol. 20, pp. 22278–22283, 2012.
- [28] P. Sethi, A. Haldar, and S. K. Selvaraja, "Ultra-compact low-loss broadband waveguide taper in silicon-on-insulator," *Opt. Exp.*, vol. 25, pp. 10196–10203, 2017.

- [29] G. Dabos, N. Pleros, and D. Tsiokos, "Low back-reflection CMOS-compatible grating coupler for perfectly vertical coupling," *Proc. SPIE*, vol. 9367, 2015, Art. no. 936711.
- [30] J. Yao *et al.*, "A CMOS-compatible low back reflection grating coupler for on-chip laser sources integration," in *Proc. Opt. Fiber Commun. Conf.*, Anaheim, CA, USA, 2016, pp. 1–3.
- [31] A. Michaels and E. Yablonovitch, "Inverse design of near unity efficiency perfectly vertical grating couplers," *Opt. Exp.*, vol. 26, pp. 4766–4779, 2018.
- [32] T. Watanabe, M. Ayata, U. Koch, Y. Fedoryshyn, and J. Leuthold, "Perpendicular grating coupler based on a blazed antiback-reflection structure," *J. Lightw. Technol.*, vol. 35, no. 21, pp. 4663–4669, Nov. 2017.
- [33] G. Dabos, N. Pleros, and D. Tsiokos, "Ultra-low loss fully-etched grating couplers for perfectly vertical coupling compatible with DUV lithography tools," *Proc. SPIE*, vol. 9752, 2016, Art. no. 975212.
- [34] J. M. Ward, A. Maimaiti, V. H. Le, and S. N. Chormaic, "Optical micro- and nanofiber pulling rig," *Rev. Sci. Instrum.*, vol. 85, no. 11, Oct. 2014, Art. no. 111501.
- [35] R. Garcia-Fernandez *et al.*, "Optical nanofibers and spectroscopy," *Appl. Phys. B*, vol. 105, pp. 3–15, 2011.
- [36] Y. Morozov, A. Lapchuk, M. Fu, A. Kryuchyn, H. Huang, and Z. Le, "Numerical analysis of end-fire coupling of surface plasmon polaritons in a metal-insulator-metal waveguide using a simple photoplastic connector," *Photon. Res.*, vol. 6, pp. 149–156, 2018.
- [37] M. Clemens and T. Weiland, "Discrete electromagnetism with the finite integration technique," *Progr. Electromagn. Res.*, vol. 32, pp. 65–87, 2001.
- [38] S. Sederberg, C. J. Firby, S. R. Greig, and A. Y. Elezzabi, "Integrated nanoplasmonic waveguides for magnetic, nonlinear, and strong-field devices," *Nanophotonics*, vol. 6, pp. 235–257, 2016.
- [39] V. F. Fusco, *Microwave Circuits: Analysis and Computer-Aided Design*. Englewood Cliffs, NJ, USA: Prentice-Hall, 1987.
- [40] D. M. Pozar, *Microwave Engineering*. Hoboken, NJ, USA: Wiley, 2012.
- [41] A. S. Lapchuk, D. Shin, H.-S. Jeong, C. S. Kyong, and D.-I. Shin, "Mode propagation in optical nanowaveguides with dielectric cores and surrounding metal layers," *Appl. Opt.*, vol. 44, pp. 7522–7531, 2005.
- [42] R. Gordon, "Light in a subwavelength slit in a metal: Propagation and reflection," *Phys. Rev. B*, vol. 73, 2006, Art. no. 153405.
- [43] M. O. Sallam, G. A. E. Vandenbosch, G. Gielen, and E. A. Soliman, "Integral equations formulation of plasmonic transmission lines," *Opt. Exp.*, vol. 22, pp. 22388–22402, 2014.
- [44] J. S. Huang, "Design-in reliability for modern wavelength-division multiplex (WDM) distributed feedback (DFB) InP lasers," *Appl. Phys. Res.*, vol. 4, pp. 15–28, 2012.
- [45] S. Liu, T. Komljenovic, S. Srinivasan, E. Norberg, G. Fish, and J. E. Bowers, "Characterization of a fully integrated heterogeneous silicon/III-V colliding pulse mode-locked laser with on-chip feedback," *Opt. Exp.*, vol. 26, pp. 9714–9723, 2018.
- [46] L. Vivien and L. Pavesi, *Handbook of Silicon Photonics*. Boca Raton, FL, USA: CRC Press, 2013.
- [47] Y. A. Vlasov and S. J. McNab, "Losses in single-mode silicon-on-insulator strip waveguides and bends," *Opt. Exp.*, vol. 12, pp. 1622–1631, 2004.
- [48] E. M. Muellner, G. Koppitsch, J. Kraft, F. Schrank, and R. Hainberger, "CMOS-compatible Si₃N₄ waveguides for optical biosensing," *Procedia Eng.*, vol. 120, pp. 578–581, 2015.
- [49] Y. Huang, Q. Zhao, L. Kamyab, A. Rostami, F. Capolino, and O. Boyraz, "Sub-micron silicon nitride waveguide fabrication using conventional optical lithography," *Opt. Exp.*, vol. 23, pp. 6780–6786, 2015.
- [50] S. Fardini, B. Esfandyarpour, and S. Mohajerzadeh, "Anomalous anisotropic etching of (111) and (100) silicon wafers using acidic solutions," *J. Electrochem. Soc.*, vol. 153, pp. G721–G725, 2006.
- [51] R. Oosterbroek *et al.*, "Etching methodologies in <111>-oriented silicon wafers," *J. Microelectromech. Syst.*, vol. 9, pp. 390–398, 2000.
- [52] H. Lorenz, M. Despont, N. Fahrni, J. Brugger, P. Vettiger, and P. Renaud, "High-aspect-ratio, ultrathick, negative-tone near-UV photoresist and its applications for MEMS," *Sens. Actuators A, Phys.*, vol. 64, pp. 33–39, 1998.
- [53] A. E. J. Lim *et al.*, "Review of silicon photonics foundry efforts," *IEEE J. Sel. Topics Quantum Electron.*, vol. 20, no. 4, pp. 405–416, Jul./Aug. 2014.
- [54] T. Horikawa, D. Shimura, S.-H. Jeong, M. Tokushima, K. Kinoshita, and T. Mogami, "Process control and monitoring in device fabrication for optical interconnection using silicon photonics technology," in *Proc. IEEE Int. Interconnect Technol. Conf. Mater. Adv. Metallization Conf.*, 2015, pp. 277–280.
- [55] K. Vynck *et al.*, "Ultrafast perturbation maps as a quantitative tool for testing of multi-port photonic devices," *Nature Commun.*, vol. 9, 2018, Art. no. 2246.
- [56] G. Roelkens, D. van Thourhout, and R. Baets, "High efficiency silicon-on-insulator grating coupler based on a poly-silicon overlay," *Opt. Exp.*, vol. 14, pp. 11622–11630, 2006.
- [57] H.-L. Tseng, E. Chen, H. Rong, and N. Na, "High-performance silicon-on-insulator grating coupler with completely vertical emission," *Opt. Exp.*, vol. 23, pp. 24433–24439, 2015.